Check for updates

Non-monotonic frictional behavior in the lubricated sliding of soft patterned surfaces

Arash Kargar-Estahbanati [ID] and Bhargav Rallabandi [ID] *

We study the lubricated contact of sliding soft surfaces that are locally patterned but globally cylindrical, held together under an external normal force. We consider gently engineered sinusoidal patterns with small slopes. Three dimensionless parameters govern the system: a speed, and the amplitude and wavelength of the pattern. Using numerical solutions of the Reynolds lubrication equation, we investigate the effects of these dimensionless parameters on key variables such as contact pressure and the coefficient of friction of the lubricated system. For small pattern amplitudes, the coefficient of friction increases with the amplitude. However, our findings reveal that increasing pattern amplitude beyond a critical value can decrease the friction coefficient, a result that contradicts conventional intuition and classical studies on the lubrication of rigid surfaces. For very large amplitudes, we show that the coefficient of friction drops even below the corresponding smooth case. We support these observations with a combination of perturbation theory and physical arguments, identifying scaling laws for large and small speeds, and for large and small pattern amplitudes. This study provides a quantitative understanding of friction in the contact of soft, wet objects and lays theoretical foundations for incorporating the friction coefficient into haptic feedback systems in soft robotics and haptic engineering.

1 Introduction

A lubricant, a viscous liquid separating two moving objects in close contact, plays a vital role in lowering friction and extending the lifespan of engineering components.[1–3] The growing number of applications of soft materials in recent years has drawn renewed interest in "soft lubrication". For fluid-separated soft objects in close proximity to each other, the pressure due to flow is sufficiently strong to significantly deform at least one of the contacting surfaces.[4,5] This lets the lubricated film support external forces and torques.[6] This phenomenon holds significance in various areas, including the study of soft robotic grippers,[7] prosthetic synovial joints,[8] and the interaction between eyeballs and contact lenses.[9] A characteristic feature of these systems is that the thickness of the separating fluid film is set dynamically by the relative velocity between the surfaces (faster motion typically leads to thicker films).

Soft lubricated systems typically reside in one of three distinct regimes: the "boundary regime", where the lubricant is too thin to support any load, and most of the load is borne by localized dry contacts; the "mixed regime", where the lubricant partially supports the load, but some portion is still carried by dry solid-to-solid contact; and the "elastohydrodynamic lubrication" (EHL) regime, where a robust film completely separates the contacting surfaces. The transition to the EHL regime typically

Department of Mechanical Engineering, University of California, Riverside, California, 92521, USA. E-mail: bhargav@engr.ucr.edu

occurs when the film thickness is 3–8 times the typical surface roughness, and may involve surface instabilities.[10] This study focuses exclusively on the EHL regime, characterized by the absence of solid–solid contact between lubricated surfaces.[11,12]

The strong coupling between the elasticity of the contacting bodies and the flow of the lubricating fluid enables EHL systems to withstand both normal and tangential forces. However, this connection adds complexity to the analysis of such systems and typically require numerical methods except under certain limiting conditions.[13,14] In the case of small normal loads, referred to as "the non-conformal regime", the surfaces move with a relatively thick fluid film, experiencing small deformation.[4,15] Conversely, for large normal forces, the geometry resembles classical Hertzian contact, separated by a thin fluid film in what is termed the "conformal contact regime".[16,17] There may be a transition between the two regimes depending on the flow speed. Additionally, it is common to use different elastic formulations for the soft material depending on the thickness of the soft substrate relative to the flow length scale. The widely-used Winkler model is best suited to thin, compressible soft coatings,[4,16] while for very thick materials, it is typical to treat the soft material as an elastic half-space.[18,19] More sophisticated analyses for intermediate thickness bridge the gap between these limits.[20,21] In experimental studies, atomic force microscopy and a non-contacting probe have been used to measure EHL forces,[22,23] while optical interferometry have characterized fluid film thickness and soft surface deformation profiles.[5,24]

Many studies have focused on the measurement of effective friction force between lubricated soft surfaces. Previous studies
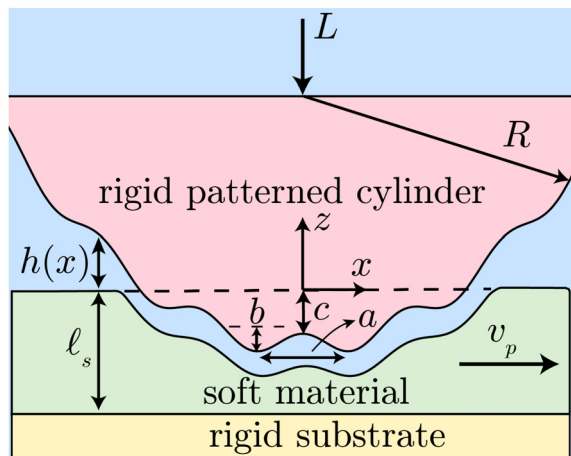
Fig. 1 Sketch of the geometry and coordinates; a patterned surface with asperities is submerged in a fluid and pressed into a deformable soft coating, which is moving to the right. The dashed line represents the original, undeformed position of the soft coating.

have observed that altering surface architecture, for example, by adding geometric micropatterns[25–28] or periodically modifying stiffness,[29–31] profoundly influences tribological performance of soft lubricated contacts. Additionally, soft surfaces in nature often exhibit roughness at the nanoscale,[32] underscoring the importance of understanding frictional behavior of lubricated uneven surfaces in fields like soft robotics,[33] and haptic engineering.[34] Experiments have found that surface asperities affect the shape of the lubricating film[35,36] as well as the transmission of forces.[7,37] Peng *et al.*,[7] in particular, showed that the friction between soft surfaces with engineered surface patterns appears to depend non-monotonically on the sliding speed. Wu *et al.* (2022)[31] undertook a numerical study for surfaces with periodically varying stiffness, correlating the additional friction force with increased energy dissipation compared to smooth surfaces. However, a systematic computational and theoretical analysis of the effect of geometrical patterns of the EHL films and force transmission is lacking.

In this study, we investigate the elastohydrodynamic lubrication of surfaces with engineered geometric patterns by developing numerical solutions to the coupled fluid-elastic problem. Focusing on sinusoidal patterns on a two-dimensional cylindrical contact geometry, we study the effect of sliding speed, the wavelength and amplitude of the pattern. Of particular interest is the effective coefficient of friction (the ratio between the EHL drag and the applied normal load). Our findings show that for small pattern amplitudes the friction increases with the square of the amplitude, while for very large amplitudes, the friction coefficient decreases as amplitude increases. We explore the physical underpinnings of this non-trivial observation using scaling analysis and perturbation theory.

2 Problem formulation

2.1 Setup and governing equations

We consider the sliding motion of a patterned rigid cylinder pressed into a rigid plane coated with an elastic material of thickness ℓ_s under a normal load L (per length of the cylinder). The two surfaces are submerged in a Newtonian fluid with viscosity η, and the bottom surface translates from left to right with velocity v_p, as depicted in Fig. 1. We assume the coating to be linear elastic with shear modulus G and Poisson's ratio ν. Relative motion establishes a layer of fluid with thickness $h(x)$ between the bodies, forming a "lubricated contact". The cylinder radius R is considerably larger than the fluid film thickness $h(x)$. We also focus our attention to sinusoidal patterns of amplitude $b/2$ and half-wavelength a, though more general patterns have been studied in experiments and modeling efforts.[7,32,36]

The flow is assumed to be incompressible and the effects of inertia are assumed negligible. We further consider gently varying patterns such that $b \ll a$. Thus, we describe the flow using lubrication theory, where the fluid velocity in the thin film is

$$v_x = \frac{1}{2\eta}\frac{\partial p}{\partial x}(z+\delta)(z+\delta-h) + v_p\left(1 - \frac{z+\delta}{h}\right), \quad (1)$$

where $p(x,t)$ is the fluid pressure and $\delta(x,t)$ is deformation of the elastic coating (positive when the coating is depressed). Integrating (1) across the fluid gap and applying the conservation of mass leads to the Reynolds lubrication equation for the pressure,[38]

$$\frac{\partial}{\partial x}\left(\frac{h^3}{\eta}\frac{\partial p}{\partial x} - 6v_p h\right) = 12\frac{\partial h}{\partial t}. \quad (2)$$

The film thickness $h(x,t)$ is a function of deformation $\delta(x,t)$ and geometry of the pattered cylindrical surface. As the surfaces are pressed together, the nominal cylindrical surface penetrates the coating a distance $c < \ell_s$. Using the standard parabolic approximation of the cylinder, valid around the central axis ($x = 0$), the top surface is at a location $z = h_{top}(x) = x^2/(2R) + (b/2)\cos(\pi x/a) - c$, while the surface of the deformed elastic coating is at $z = -\delta(x,t)$. Thus, the film thickness is

$$h(x,t) = \frac{x^2}{2R} + \frac{b}{2}\cos\frac{\pi x}{a} - c + \delta(x,t). \quad (3)$$

We note that the "penetration depth" c depends on the sliding speed and is determined dynamically as part of the solution. It is positive for static "dry" contact and small sliding speeds (as shown in Fig. 1) and may become negative at large speeds, corresponding to a cylinder that sits "raised above" the coating with a clearance between the undeformed surfaces. We note that for (2) to be valid, the surface profile must vary gently ($b \ll a$). We also focus exclusively on the EHL regime (fully separated surfaces) and so implicitly assume that the scales of the surface patterns are much greater than any nanoscale surface roughness.

The deformation $\delta(x,t)$ is related to the fluid pressure $p(x,t)$ *via* the elastic response of soft substrate. We focus here on thin compressible elastic coatings of thickness $\ell_s \ll \sqrt{R|c|}$, which have recently been realized experimentally.[5,39] In these systems, the surface deformation at any point on the coating is approximately linear in the local fluid pressure at the same point[40]

$$\delta(x,t) = Kp(x,t), \quad \text{where } K = \frac{\ell_s(1-2\nu)}{2G(1-\nu)} \quad (4)$$

is the Winkler elastic compliance. The Winkler approximation

(4) is formally valid when the deformation is small compared with thickness of the material, which in turn is smaller than the wavelength of the pattern ($\delta \ll \ell_s \ll a$). The maximum deformation is set by the penetration depth c in the limit of dry contact. Previous work has shown that the combination of the Winkler approximation and lubrication theory is in good quantitative agreement with experiments with smooth cylinders of centimetric radii.[5,39,41] We therefore anticipate that the inclusion of gentle surface undulations in the modeling framework, as is done here, will yield similarly accurate quantitative insights under similar experimental conditions. Furthermore, the Winkler approximation (with an appropriate choice of K) often provides qualitatively similar results to more sophisticated elastic descriptions in coupled fluid-elastic systems,[16,42] and serves as a useful model in a rather wide range of soft matter systems.[43]

Subject to vanishing condition for pressure far outside the film ($p(\pm\infty) = 0$), eqn (2) and (3) yield a system of equations for $p(x,t)$ and $h(x,t)$. In addition, the penetration depth c must be determined self consistently such that the stress of the flow counteracts the applied normal load (per length) L,

$$L = \int_{-\infty}^{\infty} p \, dx. \qquad (5)$$

The system of eqn (2)–(5), once solved simultaneously, yield the pressure $p(x,t)$, film thickness $h(x,t)$ and penetration depth c in terms of v_p, L, and the mechanical and geometrical properties of the system.

In the static limit with $v_p = 0$, the fluid drains from the gap between the contacting surfaces, resulting in $h(x,t) = 0$. Thus, eqn (3) becomes independent of the lubrication eqn (2). This scenario, known as "dry contact", requires solving (3)–(5) simultaneously to determine pressure $p(x)$ and penetration depth c (see ref. 40 for details). We later use the dry contact problem to evaluate the quasi-static limit, where the relative velocity is small, and the fluid film is extremely thin.

2.2 Non-dimensionalization

We rescale the governing equations before solving the problem, using the "dry" static contact problem in the smooth limit ($b = 0$) to identify characteristic length and pressure scales. This limit admits an analytic solution. The two surfaces make contact in the region $-\ell < x < \ell$, where

$$\ell = \left(\frac{3LR\ell_s}{4G} \frac{1 - 2\nu}{1 - \nu} \right)^{1/3} \qquad (6)$$

is the half-length of static contact. The contact pressure distribution in this limit is

$$p(x) = \frac{3L}{4\ell} \left(1 - \frac{x^2}{\ell^2} \right) \quad \text{(smooth, dry).} \qquad (7)$$

Thus, in the dry, smooth limit, the total contact length is 2ℓ, the maximum pressure is $\dfrac{3L}{4\ell}$, and the vertical length scale (which sets the magnitude of c) is $\ell^2/2R$. We use these scales to define

dimensionless quantities (denoted with overbars) as follows:

$$\bar{x} = \frac{x}{\ell}, \quad \bar{h} = \frac{h}{\ell^2/(2R)}, \quad \bar{c} = \frac{c}{\ell^2/(2R)}, \quad \bar{p} = \frac{p}{3L/4\ell}. \qquad (8)$$

Substituting these scales into the Reynolds equation identifies a dimensionless velocity

$$\lambda = \frac{32\eta v_p R^2}{L\ell^2} = \frac{2^{19/3}}{3^{2/3}} \frac{\eta v_p R^{4/3}}{L^{5/3}\ell_s^{2/3}} \left(\frac{G(1-\nu)}{1-2\nu} \right)^{2/3}. \qquad (9)$$

In general, transient effects may be important in the study of EHL film formation between textured surfaces.[25–27] In the present setup, the bottom surface is planar when undeformed, so the system admits a steady state in the reference frame of the cylinder (see Fig. 1). We focus on this steady state, where the system of governing eqn (2)–(5) rescale as

$$\frac{\partial}{\partial \bar{x}} \left(\bar{h}^3 \frac{\partial \bar{p}}{\partial \bar{x}} - \lambda \bar{h} \right) = 0, \qquad (10a)$$

$$\bar{h}(\bar{x}) = \bar{p} + \bar{x}^2 + \frac{\beta}{2} \cos \frac{\pi \bar{x}}{\alpha} - \bar{c}, \qquad (10b)$$

$$\int_{-\infty}^{\infty} \bar{p} \, d\bar{x} = \frac{4}{3}, \qquad (10c)$$

where $\beta = 2Rb/\ell^2$ and $\alpha = a/\ell$ are rescaled pattern amplitude and half-wavelength, respectively. The condition of gentle surface variation—previously noted—translates into $\beta \ll \alpha R/\ell$ in terms of dimensionless parameters. In this study, we focus on pattern amplitudes comparable to the dry penetration depth, i.e., $\beta = O(1)$.

We solve the system of equations (10) by initially guessing a value for penetration depth $\bar{c}$. The eqn (10a) and (10b), which yield a second-order nonlinear ODE subjected to $\bar{p}(\pm\infty) = 0$, are solved using the shooting method so that the pressure decays to zero at both ends of the computational domain. Due to the multiple scales of the problem, precise resolution is needed in regions of high curvature, while other regions can be resolved with a coarser grid. We therefore employed MATLAB's ODE45 solver, which automatically generates a non-uniform grid based on error tolerance and solution smoothness. The next section demonstrates that the solution profile supports this approach. At this stage the solution only satisfies the flow eqn (10a), while the normal load balance (10c) is not yet met. Therefore, we iterate on $\bar{c}$ (re-solving the lubrication problem each time) to satisfy (10c) within a small tolerance, completing a solution to the system (10) for a prescribed set of λ, α and β.

3 Results and discussion

3.1 Pressure and film thickness

We examine solutions of the system of eqn (10), the rescaled pressure ($p/(3L/4\ell)$), and the rescaled film thickness ($h/(\ell^2/2R)$) across a range of dimensionless parameters λ, α, and β. Fig. 2(a) and (b) plots the fluid film thickness ($\bar{h}$) and pressure ($\bar{p}$) as functions of the horizontal coordinate ($\bar{x}$) for different values of normalized speed (λ). The pattern amplitude β and the rescaled
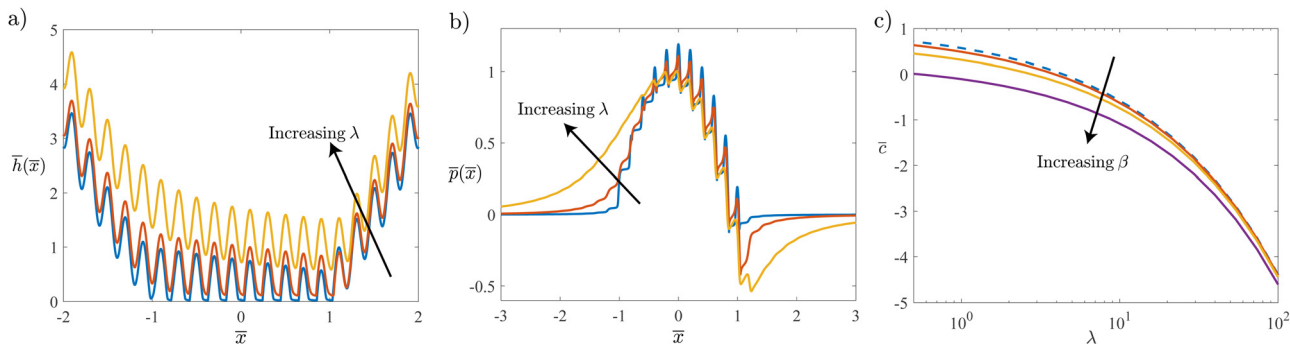
Fig. 2 (a) Dimensionless film thickness ($\bar{h}$) and (b) dimensionless pressure ($\bar{p}$) plotted against the dimensionless horizontal coordinate ($\bar{x}$) for various values of normalized speed $\lambda = 5$, 0.5 and 0.05. $\beta = 1$ for both (a) and (b); and (c) dimensionless penetration depth ($\bar{c}$) *versus* dimensionless speed (λ) for various values of dimensionless pattern amplitude $\beta = 0$, 0.5, 1.0 and 2.0. Throughout the figure, $\alpha = 0.1$.

pattern wavelength α are constant throughout Fig. 2. The variables $\bar{p}$ and $\bar{h}$ are directly derived from the numerical solution of (10), and the precision of their calculation determines the accuracy of our results. Thus, a mesh study was performed to assure that the final solution is converged. Fig. 2 confirms that the problem has multiple scales, necessitating a non-uniform mesh to accurately resolve the profile. For small λ, representing a small speed or a large normal load, the fluid film thickness and pressure distribution are strongly influenced by the amplitude. In particular, we see localized regions with large pressure and very thin films (small $\bar{h}$), which correspond to the regions of contact inherited from the static problem. These are separated by "gaps" where the fluid film is much thicker. For large speeds ($\lambda \gg 1$) by contrast, $\bar{h}$ significantly exceeds β. Consequently, the solution to the elastohydrodynamic problem predominantly mirrors the smooth-cylinder solution, augmented by relatively minor fluctuations resulting from the sinusoidal protrusions. The independence of the solution for large values of β is also seen in Fig. 2(c), which plots the penetration depth $\bar{c}$ *versus* the speed λ for different β.

3.2 Coefficient of friction

As noted earlier, the primary objective of this study is to understand the effect of pattern amplitude on the coefficient of friction μ, defined as the ratio of the EHL drag D to the applied load L. From solutions of the pressure and film thickness, μ is found as

$$\mu = \frac{D}{L} = \frac{1}{L} \int \left(-p \frac{\partial h}{\partial x} - \eta \frac{\partial v}{\partial z} \bigg|_{z=h_{\text{top}}} \right) dx \tag{11a}$$

$$= \frac{\ell}{2R} \frac{\int \frac{1}{2} \bar{h} \frac{\partial \bar{p}}{\partial \bar{x}} - \frac{\lambda}{6\bar{h}} + \frac{\partial \bar{h}_{\text{top}}}{\partial \bar{x}} \bar{p} \, d\bar{x}}{4/3}, \tag{11b}$$

where (11b) uses rescaled variables. We note that since the load is held constant throughout in the present formulation (independent of the parameters α, β and λ), the coefficient of friction is simply a rescaled version of the drag.

We first study the effect of the pattern amplitude and wavelength on the friction coefficient. The wavelength of the

protrusions 2α evidently affects the spatial structure of the pressure and film thickness distributions (Fig. 2). However, we find that the wavelength has only a weak effect on the friction coefficient, particularly when it is much smaller than the contact length ($\alpha \ll 1$), as illustrated in Fig. 3(a). A similar independence of forces on the wavelength of surface patterns was shown to hold (using formal asymptotic arguments and validated numerically) in the context of rigid surfaces with sinusoidal undulations.[44] Later, we offer a rationalization of
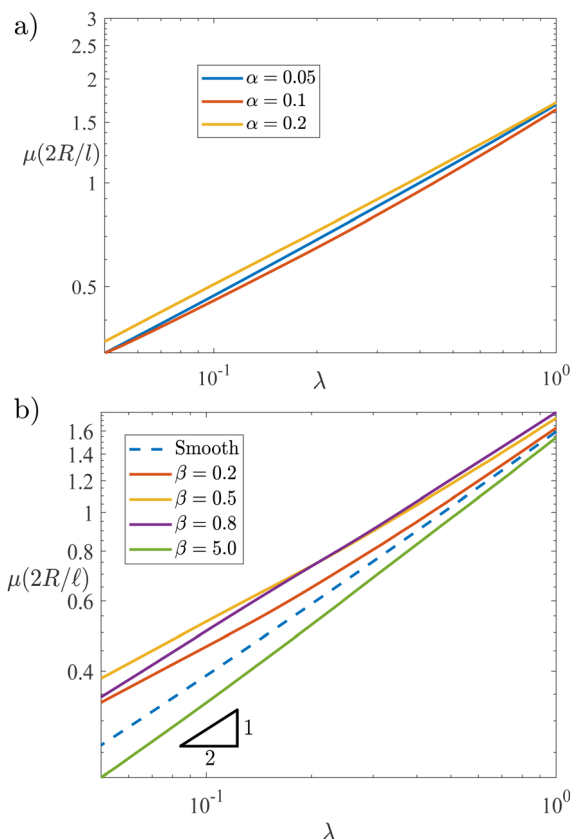

Fig. 3 (a) Friction coefficient (μ) *versus* dimensionless speed (λ) for different values of dimensionless wave length (α), $\beta = 0.2$ (b) Friction coefficient (μ) *versus* dimensionless speed (λ) for different values of amplitude (β), $\alpha = 0.1$.
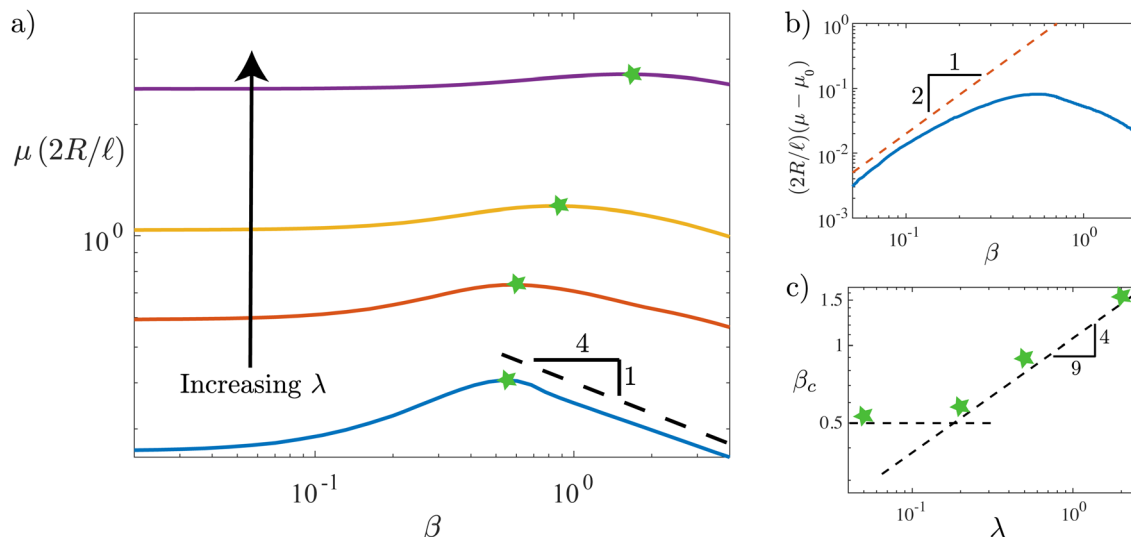
Fig. 4 (a) Friction coefficient *versus* amplitude (β) for different values of dimensionless speed λ = 0.05, 0.2, 0.5, 2.0. Stars represent the maximum friction at each speed. (b) Difference between the friction coefficients in the rough and smooth cases ($\mu - \mu_0$) for small pattern amplitude $\beta \ll 1$. The solid curve shows the numerical results, while the dashed curve represents a scaling analysis. (c) The critical pattern amplitude β_c (maximizing friction) grows as a function of the speed λ. Dashed lines show predicted scaling behaviors at small and moderate speeds.

this independence using scaling and symmetry arguments, accounting for deformations. We note that the condition of small wavelength is natural in the context of "surface textures", whereas the case $\alpha = O(1)$ modifies the cylindrical shape across the entire lubricated film region and is not the regime of interest here. We thus work in the small-wavelength regime throughout the paper, focusing on the dependence of μ on the remaining dimensionless parameters, λ and β.

Fig. 3(b) studies the influence of dimensionless speed λ on friction coefficient for different values of the rescaled surface amplitude β. For a smooth cylinder at small λ, a balance between the O(1) pressure gradient, determined by dry contact, and the viscous stress in (10a), suggests a film thickness scaling of $\bar{h}_0^* \propto \lambda^{1/2}$ (see also ref. 42). By substituting the film thickness and pressure scaling into (11b), the friction coefficient is found to scale as $\mu \propto (\ell/2R)\lambda^{1/2}$. This scaling with λ is consistent with the numerical results for $\beta = 0$, shown in Fig. 3(b). As the pattern amplitude β increases from zero at a fixed speed λ, the friction coefficient increases, aligning with both experimental observations[7] and intuitive expectations. However, the opposite is observed for sufficiently large β – the coefficient of friction decreases with increasing amplitude. This non-monotonic dependence of the friction on the pattern amplitude is most noticeable for small and moderate speeds λ, where the deformation of the solid is comparable to (or greater than) the film thickness; compare the curves for $\beta = 0.8$ and $\beta = 0.5$ in Fig. 3(b). Surprisingly, for very large β, the coefficient of friction can drop to values even below the smooth limit ($\beta = 5$ curve in Fig. 3(b)).

To illustrate this counter-intuitive behavior more clearly, in Fig. 4(a) we plot the rescaled friction coefficient $\mu(2R/\ell)$ *versus* amplitude β. Starting from a smooth surface ($\beta = 0$), increasing amplitude β first results in an increase in the friction coefficient (see also Fig. 4(b)). For a fixed λ, the maximum friction occurs at critical value $\beta = \beta_c$, indicated by star symbols in

Fig. 4(a). Increasing the pattern height beyond β_c lowers the friction coefficient. Eventually, μ falls below its smooth limit. As λ increases, the value of β_c increases (Fig. 4(a) and (c)), while the height of the maximum itself diminishes. These features seem to persist for larger λ but become less prominent. We analyze these features in the following sections, focusing separately the limits of large and small values of either β or λ.

3.3 Friction at low speeds: scaling analysis

We first consider the limit of small λ, which displays the strongest dependence of μ on β. For small β, it is useful to perturb around the smooth solution, where the film thickness is $\bar{h}_0(\bar{x})$ and has a characteristic scale $\bar{h}_0^*$. For $\beta \ll \bar{h}_0^*$, we expect that the film thickness takes the shape $\bar{h}(\bar{x}) = \bar{h}_0(\bar{x})\left(1 + \sigma \mathscr{S} + \sigma^2 \mathscr{S}^2 + O(\sigma^3)\right)$, where $\sigma = \beta/\bar{h}_0^*$ is a small parameter (representing the ratio of the pattern amplitude to the film thickness) and $\mathscr{S}(\bar{x})$ is a sinusoidal function of O(1) amplitude and O(α) $\ll$ 1 wavelength. We now consider the contribution to the shear stress to the drag, which scales as $\int \lambda/\bar{h} \mathrm{d}\bar{x}$. We expand the integrand in powers of σ as $\int \lambda/\bar{h}_0 \left(1 + \sigma \mathscr{S} + \sigma^2 \mathscr{S}^2\right) \mathrm{d}\bar{x}$ (note that we omit prefactors in front of the powers of σ since the argument is at the level of scaling). The terms linear in σ are also linear in the rapidly oscillating sinusoid $\mathscr{S}(\bar{x})$, so it integrates to zero. The first nonzero amplitude contribution results from the term involving O($\sigma^2 \mathscr{S}^2$), which on integration yields a term of O(σ^2) that is independent of α (this independence occurs because the integral picks out the zero-wavenumber Fourier component of $\mathscr{S}^2$). A similar symmetry argument also applies to terms involving the pressure. Thus, we expect that the coefficient of friction for small β takes the form

$$\mu \sim \mu_0 \left(1 + k\left(\frac{\beta}{\bar{h}_0^*}\right)^2\right) \text{ for } \beta \ll \bar{h}_0^*, \quad (12)$$

where μ_0 is the smooth ($\beta = 0$) limit, and the prefactor k results from the detailed integration. As noted earlier in the text, $\bar{h}_0^* \propto \lambda^{1/2}$ and $\mu_0 \propto (\ell/2R)\lambda^{1/2}$. Substituting these expressions into (12), we expect that the friction coefficient for small β and small λ behaves as

$$\mu \sim \frac{\ell}{2R}\left(k_1\lambda^{1/2} + k_2\beta^2\lambda^{-1/2}\right) \text{ for } \beta \ll \lambda^{1/2} \ll 1, \quad (13)$$

for O(1) constants k_1 and k_2. The first term represents the smooth limit, while the second is the leading effect of the pattern amplitude. The difference between the rough and smooth friction coefficients scales as β^2 for small β, in agreement with numerical calculations (Fig. 4(b)).

We now analyze the scaling behavior for large amplitude ($\beta \gg 1$), still considering small speeds ($\lambda \ll 1$). For large β, the dry contact problem is significantly different from the smooth case. The contact between the two surfaces is no longer contiguous, and is instead made up of n isolated contact regions, where the individual protrusions locally deform the soft substrate. These contact regions are separated by gaps between the protrusions (see Fig. 5). For large β, the contact regions are

relatively narrow and have dimensionless widths $\bar{\ell}_f \ll \alpha$, while the gaps have widths of $\bar{\ell}_f = O(\alpha)$. When motion is initiated, the contacting regions become lubricated and support thin fluid films, while the gap regions remain largely unchanged, as seen in Fig. 5(a). To understand the contributions of the two kinds of regions on the force, we define the cumulative drag and lift functions, respectively,

$$\mathscr{D}(\bar{x}) = \int_{-\infty}^{\bar{x}}\left(\frac{1}{2}\bar{h}\frac{\partial\bar{p}}{\partial\bar{x}} - \frac{\lambda}{6\bar{h}} + \frac{\partial\bar{h}_{\text{top}}}{\partial\bar{x}}\right)ds \quad (14)$$

$$\mathscr{L}(\bar{x}) = \int_{-\infty}^{\bar{x}}\bar{p}ds, \quad (15)$$

where the integrands are functions of the "dummy" spatial variable s. Note that by definition $\mathscr{D}(\infty) = D$ and $\mathscr{L}(\infty) = 4/3$.

Fig. 6 shows the accumulation of drag and lift forces in both the film and gap regions for $\lambda = 0.05$, $\beta = 4$. It is clear that the drag is accumulated in the n thin films of length $\bar{\ell}_f$ corresponding to initially dry contact. These are regions of high shear stress (due to thin films) whereas the gaps have much thicker
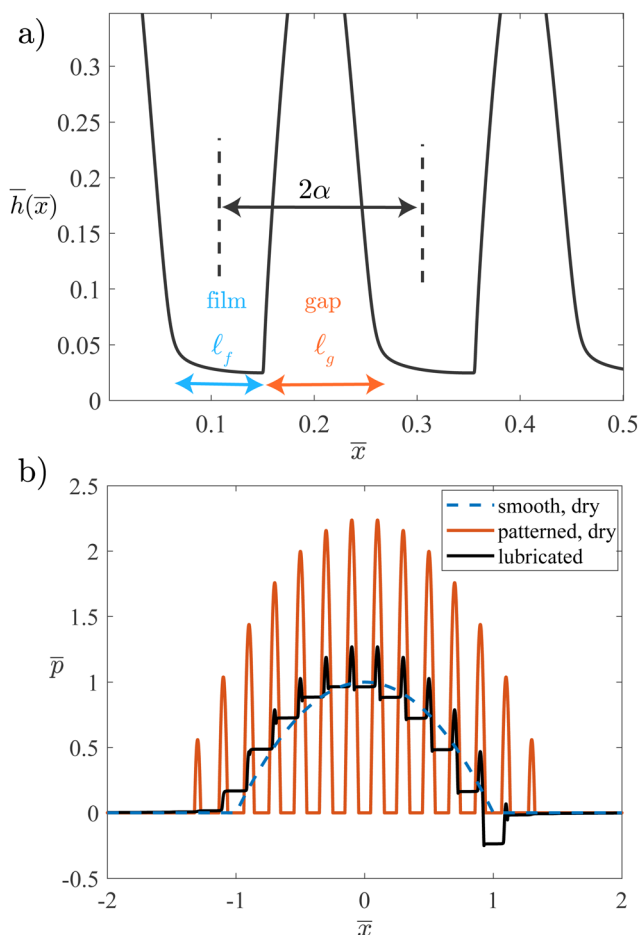

Fig. 5 (a) A zoomed-in plot of the film thickness for $\beta = 1.6$ and $\lambda = 0.05$, highlighting the film and gap regions. (b) Dimensionless pressure $\bar{p}$ versus dimensionless horizontal coordinate $\bar{x}$ for the $\beta = 4$ and $\lambda = 0.05$, the corresponding dry contact, and the dry smooth contact.
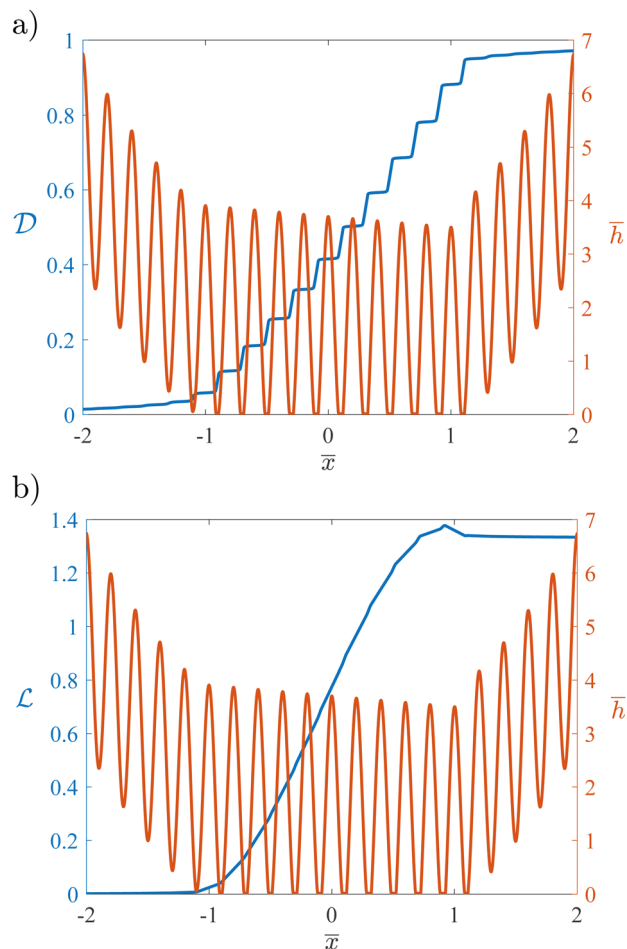

Fig. 6 Plot of cumulative dimensionless forces: (a) drag force and (b) lift force in blue, together with film thickness $\bar{h}$ in red as a function of dimensionless horizontal coordinate ($\bar{x}$) for $\lambda = 0.05$ and $\beta = 4.0$. The plots feature two vertical axes: the left axis indicates the cumulative integral values, while the right axis displays the dimensionless film thickness $\bar{h}$.

films and thus much lower stress. In contrast to the drag, the lift is accumulated gradually across the entire "contact region" of dimensionless length $\bar{\ell}_f \sim 1$, encompassing both gap and film regions. Since the films are much narrower than the gaps, most of the lift is therefore supported by the pressure in the gaps. Using (5) to balance normal stresses with the applied load suggests a pressure scale of $O(L/\ell)$. In dimensionless terms, we thus expect $\bar{p} = O(1)$ and $d\bar{p}/d\bar{x} = O(1)$ for the lubricated problem. We verify this conclusion by plotting the pressure for $\beta = 4$ and $\lambda = 0.05$ in Fig. 5(b). Contrary to the corresponding dry contact where the pressure is concentrated in the contact regions, the pressure in the lubricated patterned case remains relatively close to the smooth problem, with smaller fluctuations in the thin-film regions. We posit that this is due to the continuous fluid film, which distributes the pressure uniformly due to continuity, requiring a constant fluid flux through the system.

We now use (2) along with the conclusion $d\bar{p}/d\bar{x} = O(1)$ to estimate the film thickness as $\bar{h} \sim \lambda^{1/2}$, valid in the thin film regions. Referring back to (11), it is easy to see that all three stress contributions in the integrand scale as $\lambda^{1/2}$ in the film regions. Recalling that the drag force is mostly accumulated in n thin-film regions, each of width $\bar{\ell}_f$ (cf. Fig. 6(a)), we conclude that the drag force scales as $\lambda^{1/2} n \bar{\ell}_f$. Referring back to Fig. 5(b), we see that the number of teeth in contact n and the length of the flat regions $\bar{\ell}_f$ in the lubricated problem are determined by the dry contact features. In the appendix, we show using scaling arguments that the dry contact is characterized by $n \sim \beta^{1/8}/\alpha$, and $\bar{\ell}_f \sim \alpha \beta^{-3/8}$. Combining these arguments, we obtain the scaling relation $D \sim \lambda^{1/2} \beta^{-1/4}$. The coefficient of friction is therefore

$$\mu \sim \frac{\ell}{2R} \lambda^{1/2} \beta^{-1/4}, \quad \text{for } \lambda \ll 1, \ \beta \gg 1, \tag{16}$$

and is validated by numerical results in Fig. 4. Notably, the prediction is also independent of α, consistent with the numerical findings shown in Fig. 3(a).

The crossover between the low-β and high-β estimates (13) and (16) yield an estimate of the critical value β_c at which the friction is maximized at a given speed. For very small β, the second term of (13) is negligible. Then, the crossover between the small-β and large-β limits occurs at $\beta_c = O(1)$, independent of λ. This corresponds to pattern heights that are comparable to the dry indentation depth. For larger β, the second term of (13) starts to become comparable to, and eventually dominate over, the first term. Then, comparing the second term of (13) with (16) yields a crossover at $\beta_c = O(\lambda^{4/9})$, which grows with λ. These scaling predictions for small and large β are consistent with the β_c obtained from numerical solutions, as seen in Fig. 4(c). As noted earlier, the film thickness grows as $\lambda^{1/2}$, so the scaling prediction $\beta_c \propto \lambda^{4/9}$ corresponds to patterns with amplitude approximately equal to the thickness of the entrained fluid film.

3.4 Friction at high speeds: perturbation theory

For large λ, the film thickness increases (Fig. 2(a)), and eventually becomes much greater than both the elastic deformation and the pattern amplitude. We thus employ a small-deformation perturbation expansion in the vein of Skotheim and Mahadevan,[4] but include the effects of the pattern. We outline the main ideas here, and present a more detailed analysis in Appendix B. For large λ, the rough cylinder floats above the undeformed surface of the bottom substrate, such that c becomes large and negative. The ratio of the deformation scale to the film thickness is $\Lambda = \eta v_p K (2R)^{1/2} |c|^{-5/2}$, which is small. Additionally, the pattern amplitude relative to the gap defines $\varepsilon = b/(2|c|)$, which is also small. We expand the governing equations in a perturbation series for small Λ (Appendix B), solve the resulting problems numerically (for different values of ε) and compute drag D and lift L forces. Separately, a small-amplitude expansion of these coefficients identifies that the drag and lift take the approximate form $D = \eta v_p (2R/|c|)^{1/2} (\mathfrak{D}_0 + \varepsilon^2 \mathfrak{D}_2)$ and $L = \Lambda \eta v_p (2R/|c|)^{1/2} (\mathfrak{L}_0 + \varepsilon^2 \mathfrak{L}_2)$, up to corrections of $O(\Lambda^2, \varepsilon^4)$ where the $\mathfrak{D}_i$ and $\mathfrak{L}_i$ are $O(1)$ parameter-independent coefficients (Appendix B). The coefficients $\mathfrak{D}_0 = 2\pi$ and $\mathfrak{L}_0 = 3\pi/8$ correspond to drag[45] and lift[4] on a smooth cylinder near a weakly deformable soft surface and are known analytically. The absence of terms linear in ε (and indeed all odd powers of ε) stems from the symmetry of the problem, as noted in Section 3.3. We then find $\mathfrak{D}_2 \approx 3\pi/2$ and $\mathfrak{L}_2 \approx 3\pi/2$ by fitting the analytic forms for D and L to our numerical force calculations.

Having obtained forces in terms of the gap height $|c|$, we recast the expression for lift in terms of the original "fixed-load" dimensionless variables to obtain

$$\frac{1}{48} \frac{\lambda^2}{|\bar{c}|^{7/2}} \left(\mathfrak{L}_0 + \frac{\beta^2}{|\bar{c}|^2} \mathfrak{L}_2 \right) = 1, \tag{17}$$

which is a nonlinear equation for $|\bar{c}|$. Substituting the small-Λ, small-ε expressions for D and L, we find after some manipulation that the coefficient of friction is

$$\mu = \frac{\ell}{2R} \frac{\lambda \left(\mathfrak{D}_0 + \mathfrak{D}_2 \frac{\beta^2}{\bar{c}^2} \right)}{8 \bar{c}^{1/2}}. \tag{18}$$

Thus, we first solve the nonlinear eqn (17) for $\bar{c}$ and then substitute these values into (18) to obtain a semi-analytic approximation for the coefficient of friction μ. A comparison of this result with the fully numerical calculation is depicted in Fig. 7 for different values of λ and β. As evident from Fig. 7(a), the results of (18), depicted by dashed lines, are in quantitative agreement with the numerical results at large λ. Moreover, the semi-analytic solution provides a reasonably accurate qualitative prediction at moderate speeds ($\lambda \approx 10$).

Furthermore, it is clear from (17) and (18) that the leading effects of pattern on μ scale with β^2. To examine the effect of amplitude on the friction coefficient, we subtracted the friction coefficient of the smooth problem, μ_0, from the total friction coefficient μ, and compared the higher-order terms in Fig. 7(b) at fixed λ. The β^2 scaling (dashed curve) is evident in the figure, with analytical results showing good agreement with numerics up to $\beta \approx 10$.
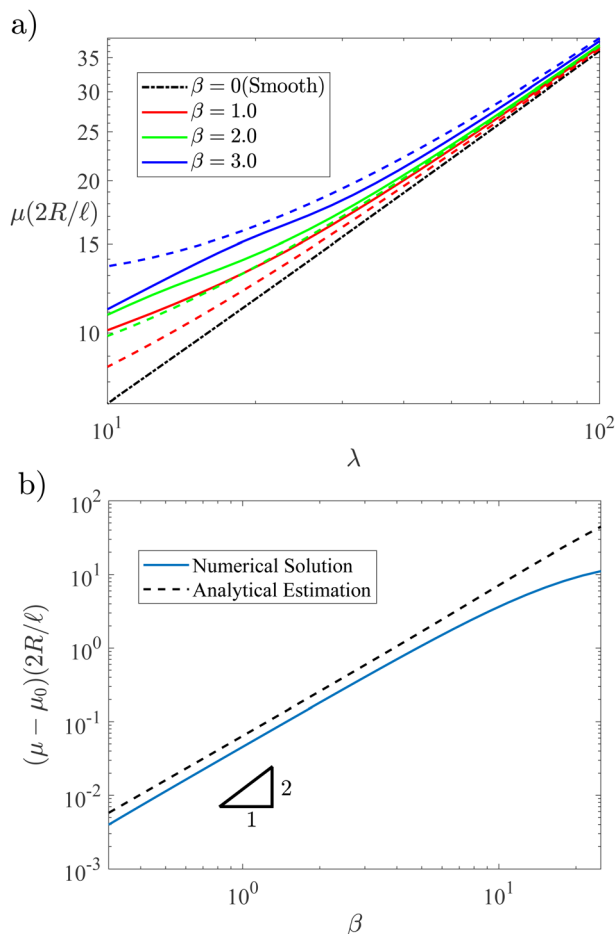
Fig. 7 (a) Rescaled friction coefficient, $\mu(2R)/\ell$, *versus* the dimensionless speed, λ. Solid lines depict the numerical results, while dashed lines illustrate the analytical predictions. (b) The deviation of the friction coefficient from the soft smooth problem, $\mu - \mu_0$, presented against the dimensionless pattern amplitude, β, for a fixed dimensionless speed of $\lambda = 1000$. $\alpha = 0.6$ throughout the figure.

4 Conclusions

We have studied the lubricated contact of a patterned curved surface on a soft coated substrate, assuming a local Winkler-type elastic description. The model is governed by three dimensionless parameters: α, the dimensionless wavelength of the patterns; β, the dimensionless pattern amplitude; and λ, the dimensionless relative speed of the contacting surfaces. Numerical solutions and symmetry arguments show that the effective (lubricated) coefficient of friction is insensitive to variations in α for small α.

An interesting and nontrivial finding is that the coefficient of friction depends non-monotonically on the pattern amplitude at fixed speeds. For small amplitudes, the friction coefficient grows from the smooth case proportional to β^2, which we understand using symmetry arguments. For large pattern amplitudes, the friction coefficient decreases as $\beta^{-1/4}$, eventually becoming lower than even the smooth limit. We understand this behavior for small speeds by analyzing the contact geometry established in the "dry" static limit. While much of

the drag is accounted for by thin films, the applied load is counteracted by the spaces in between the films. At larger amplitudes, the fraction of contact occupied by the films decreases, leading to lower drag. At much larger speeds, a greater volume of fluid is entrained leading to thicker films, and the effects of surface patterns become weaker.

The theoretical and numerical insights provided by this work reveal interesting and non-intuitive behaviors arising from interactions between fluid flow, elasticity and the multiple length scales associated with patterned surfaces. Among these is the non-monotonic dependence of the friction coefficient on the amplitude of the pattern. This behavior is reminiscent of (albeit distinct from) the recent experimental observations of ref. 7 where a non-monotonic dependence of friction on sliding speed was observed for patterned surfaces, but was absent for smooth surfaces.

The insights identified by this work offer a deeper understanding of the role of surface patterns in the interactions of soft materials. Future work may employ a more complete elastic modeling framework, *e.g.* one valid for bulk elastic materials rather than thin compressible coatings. One may also consider the effect of patterns on both surfaces, or the effects of material viscoelasticity, both of which lead to time-dependent dynamics. While we have focused here on two-dimensional engineered surface patterns with small slopes, it would be interesting to consider the effects of more general surface profiles, including three-dimensional profiles and nanoscale roughness. The inclusion of such effects introduces additional physics such as surface instabilities and intermolecular forces,[10] providing opportunity for future modeling efforts. We envision further development of our findings to more complex geometric or material configurations, as well their use in the design of haptic and soft robotic applications.

Author contributions

A. K.-E. developed the theory and simulations. B. R. developed some scaling arguments. Both authors conceived the project, analyzed the results and wrote the paper.

Conflicts of interest

The authors have no conflicts of interest.

Appendix

A Dry contact at large β

As observed in Fig. 5(b), when $\lambda \ll 1$, the lubricated problem inherits certain features from the dry problem, such as the number of teeth in contact n, the length of flattened regions ℓ_f, and the gap regions ℓ_g. Here, we focus on the limit where β is large and study the scaling of various quantities with respect to α and β.

At dry contact, the teeth "penetrate" into the soft material a depth c. This sets up two horizontal length scales: a global "apparent contact" length scale $(Rc)^{1/2}$, and a flattened local contact scale $\ell_f \sim (r_f c)^{1/2}$ on each tooth, where r_f is the radius of curvature of the tooth. By taking the second derivative of (3), we
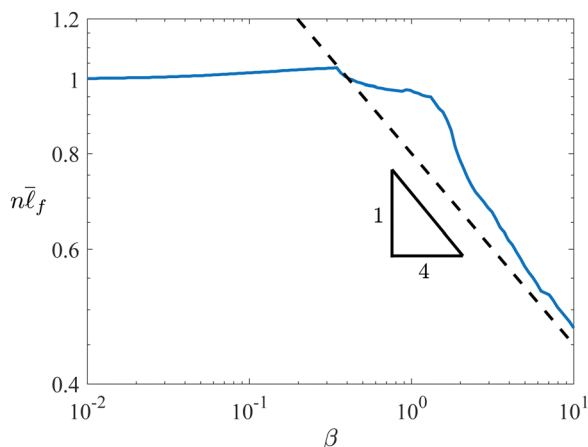
Fig. 8 Plot of $n\ell_f$ versus β for the dry contact with $\alpha = 0.1$. The solid line represents the numerical solution, while the dashed line illustrates the scaling prediction.

find that $r_f \sim a^2/b$, so the dimensionless local contact length is $\bar{\ell}_f = \ell_f/\ell \sim \alpha(\bar{c}/\beta)^{1/2}$. The global length scale is spread across n teeth a distance a apart from each other, so $(Rc)^{1/2} \sim \alpha n$, or in dimensionless terms $\bar{c}^{1/2} \sim \alpha n$. Additionally, using (10c) and considering that the load is supported by the flattened contact regions, we can express $\bar{p}\bar{\ell}_f n \sim 1$. For a Winkler-elastic solid, $\bar{p} \sim \bar{c}$. Combining these scaling relations, the geometric features of dry contact scale with α and β as

$$\bar{c} \sim \beta^{1/4}, \quad \bar{\ell}_f \sim \alpha\beta^{-3/8}, \quad n \sim \alpha^{-1}\beta^{1/8} \qquad (19)$$

Notably, the product $n\bar{\ell}_f \sim \beta^{1/4}$ (independent of α), which enters (16). To validate this scaling analysis, Fig. 8 compares $n\bar{\ell}_f$, the variable employed in the main text, from (19) with the numerical solution of the dry contact problem, obtained from solving (10b) with $\bar{h} = 0$, subject to (10c).

B   Large-λ perturbation expansion

At large λ, the film thickness is greater than both the deformation and the pattern amplitude, making the problem amenable to a perturbation analysis. Extensively discussed for smooth surfaces in existing literature,[4,42] we adapt this approach to patterned surfaces. It is convenient to reformulate the problem in terms of the separation $|c|$ rather than the load, and later translate back to the fixed-load framework introduced in Section 2. The film thickness scales with $|c|$, setting the horizontal length scale $\sqrt{2R|c|}$. The relevant pressure scale is $\eta v_p R^{1/2}|c|^{-3/2}$, which, through (4), identifies the deformation scale. Normalizing variables according to these scales leads to the rescaled lubrication equation (uppercase letters are dimensionless)

$$\frac{\partial}{\partial X}\left(H^3\frac{\partial P}{\partial X} - 6H\right) = 0. \qquad (20)$$

The fluid film thickness H is expressed in terms of pressure and geometric parameters as:

$$H(X) = 1 + X^2 + \varepsilon\cos\left(\frac{\pi X}{\hat{\alpha}}\right) + \Lambda P(X), \qquad (21)$$

where Λ is the dimensionless deformation, ε is dimensionless pattern amplitude (both defined in Section 3.4), and $\hat{\alpha} = a/\sqrt{2|c|R}$. All three parameters are small in the asymptotic sense.

We develop a perturbation expansion for $\Lambda \ll 1$, expanding pressure as $P = P_0 + \Lambda P_1 + O(\Lambda^2)$. Substituting into (21) yields

$$\Lambda^0 : \frac{\partial}{\partial X}\left(H_0^3\frac{\partial P_0(X)}{\partial X} - 6H\right) = 0, \qquad (22a)$$

$$\Lambda^1 : \frac{\partial}{\partial X}\left(H_0^3\frac{\partial P_1(X)}{\partial X} + 3H_0 P_0(X)\frac{\partial P_0(X)}{\partial X} - 6P_0(x)\right) = 0, \qquad (22b)$$

where $H_0 = 1 + X^2 + \varepsilon\cos\pi X/\hat{\alpha}$ represents the film thickness of the corresponding rigid problem ($\Lambda \to 0$). We solve (22a) and (22b) numerically for different ε. We use these solutions to compute drag and lift forces, which (here written as dimensional quantities) take the form $D = \eta v_p(2R/|c|)^{1/2}\mathfrak{D}(\varepsilon)$ and $L = \eta v_p(2R/|c|)^{1/2}\mathfrak{L}(\varepsilon)$, where $\mathfrak{D}(\varepsilon)$ and $\mathfrak{L}(\varepsilon)$ are O(1) functions that result from the numerical computation. Noting that $\varepsilon \ll 1$ for large λ we expand these functions as $\mathfrak{D} = \mathfrak{D}_0 + \varepsilon^2\mathfrak{D}_2 + \cdots$ and $\mathfrak{L} = \eta(\mathfrak{L}_0 + \varepsilon^2\mathfrak{L}_2)$. The coefficients $\mathfrak{D}_0 \approx 2\pi$ and $\mathfrak{L}_0 \approx 3\pi/8$ are well-established results in the literature[4,45] and correspond to the smooth problem. A fit to the numerical force computations determine $\mathfrak{D}_2 \approx 3\pi/2$ and $\mathfrak{L}_2 \approx 3\pi/2$.

Acknowledgements

Notes and references

1 E. H. Okrent, *ASLE Trans.*, 1961, **4**, 97–108.
2 V. Borsoff, *J. Basic Eng.*, 1959, **81**, 79–88.
3 J. A. McGeehan, *SAE Trans.*, 1978, 2619–2638.
4 J. M. Skotheim and L. Mahadevan, *Phys. Rev. Lett.*, 2004, **92**, 245509.
5 B. Saintyves, T. Jules, T. Salez and L. Mahadevan, *Proc. Natl. Acad. Sci. U. S. A.*, 2016, **113**, 5847–5849.
6 B. Rallabandi, *Annu. Rev. Fluid Mech.*, 2024, **56**, 491–519.
7 Y. Peng, C. M. Serfass, A. Kawazoe, Y. Shao, K. Gutierrez, C. N. Hill, V. J. Santos, Y. Visell and L. C. Hsiao, *Nat. Mater.*, 2021, **20**, 1707–1711.
8 J. Hou, V. C. Mow, W. Lai and M. Holmes, *J. Biomech.*, 1992, **25**, 247–259.
9 Z. Jin and D. Dowson, *Proc. Inst. Mech. Eng., Part J*, 2005, **219**, 367–380.
10 H. Dong, N. Moyle, H. Wu, C. Y. Khripin, C.-Y. Hui and A. Jagota, *Adv. Mater.*, 2023, **35**, 2211044.
11 X. Lu, M. M. Khonsari and E. R. M. Gelinck, *J. Tribol.*, 2006, **128**, 789–794.
12 B. Jacobson, *Tribol. Int.*, 2003, **36**, 781–789.

13 E. Bissett, *Proc. R. Soc. A*, 1989, **424**, 393–407.

14 E. Bissett and D. Spence, *Proc. R. Soc. A*, 1989, **424**, 409–429.

15 K. Sekimoto and L. Leibler, *Europhys. Lett.*, 1993, **23**, 113.

16 M. H. Essink, A. Pandey, S. Karpitschka, C. H. Venner and J. H. Snoeijer, *J. Fluid Mech.*, 2021, **915**, A49.

17 C.-Y. Hui, H. Wu, A. Jagota and C. Khripin, *Tribol. Lett.*, 2021, **69**, 1–17.

18 J. M. Skotheim and L. Mahadevan, *Phys. Fluids*, 2005, **17**, 092101.

19 J. H. Snoeijer, J. Eggers and C. H. Venner, *Phys. Fluids*, 2013, **25**, 101705.

20 A. Kargar-Estahbanati and B. Rallabandi, *Phys. Rev. Fluids*, 2021, **6**, 034003.

21 T. G. J. Chandler and D. Vella, *Proc. R. Soc. London, Ser. A*, 2020, **476**, 20200551.

22 S. Leroy, A. Steinberger, C. Cottin-Bizonne, F. Restagno, L. Léger and É. Charlaix, *Phys. Rev. Lett.*, 2012, **108**, 264501.

23 Z. Zhang, V. Bertin, M. Arshad, E. Raphael, T. Salez and A. Maali, *Phys. Rev. Lett.*, 2020, **124**, 054502.

24 H. S. Davies, D. Débarre, N. El Amri, C. Verdier, R. P. Richter and L. Bureau, *Phys. Rev. Lett.*, 2018, **120**, 198001.

25 C. H. Venner and A. A. Lubrecht, *J. Tribol.*, 1996, **118**, 153–161.

26 L. Mourier, D. Mazuyer, A. Lubrecht and C. Donnet, *Tribol. Int.*, 2006, **39**, 1745–1756.

27 T. Touche, J. Cayer-Barrioz and D. Mazuyer, *Tribol. Lett.*, 2016, **63**, 1–14.

28 M.-s Suh, Y.-h Chae, S.-s Kim, T. Hinoki and A. Kohyama, *Tribol. Int.*, 2010, **43**, 1508–1517.

29 N. Moyle, H. Wu, C. Khripin, F. Bremond, C.-Y. Hui and A. Jagota, *Soft Matter*, 2020, **16**, 1627–1635.

30 N. Moyle, H. Dong, H. Wu, C. Y. Khripin, C.-Y. Hui and A. Jagota, *Tribol. Lett.*, 2022, **70**, 1–12.

31 H. Wu, C. Khripin, A. Jagota and C.-Y. Hui, *Extreme Mech. Lett.*, 2022, **54**, 101735.

32 M. Ayyildiz, M. Scaraggi, O. Sirin, C. Basdogan and B. N. Persson, *Proc. Natl. Acad. Sci. U. S. A.*, 2018, **115**, 12668–12673.

33 M. J. Adams, S. A. Johnson, P. Lefèvre, V. Lévesque, V. Hayward, T. André and J.-L. Thonnard, *J. R. Soc., Interface*, 2013, **10**, 20120467.

34 C. Basdogan, F. Giraud, V. Levesque and S. Choi, *IEEE Trans. Haptics*, 2020, **13**, 450–470.

35 M. Kaneta and A. Cameron, *J. Tribol.*, 1980, **102**, 374–378.

36 J. W. Choo, A. V. Olver, H. A. Spikes, M.-L. Dumont and E. Ioannides, *J. Tribol.*, 2008, **2**, 021505.

37 A. M. Smith, C. E. Chapman, M. Deslandes, J.-S. Langlais and M.-P. Thibodeau, *Exp. Brain Res.*, 2002, **144**, 211–223.

38 L. G. Leal, *Advanced Transport Phenomena: Fluid Mechanics and Convective Transport Processes*, Cambridge University Press, 2007, vol. 7.

39 B. Saintyves, B. Rallabandi, T. Jules, J. Ault, T. Salez, C. Schönecker, H. A. Stone and L. Mahadevan, *Soft Matter*, 2020, **16**, 4000–4007.

40 K. Johnson, *Contact Mechanics*, Cambridge University Press, 1987.

41 B. Rallabandi, B. Saintyves, T. Jules, T. Salez, C. Schönecker, L. Mahadevan and H. A. Stone, *Phys. Rev. Fluids*, 2017, **2**, 074102.

42 A. Kargar-Estahbanati and B. Rallabandi, *Soft Matter*, 2022, **18**, 4887–4896.

43 D. A. Dillard, B. Mukherjee, P. Karnal, R. C. Batra and J. Frechette, *Soft Matter*, 2018, **14**, 3669–3683.

44 E. Yariv, R. Brandão, D. K. Wood, H. Szafraniec, J. M. Higgins, P. Bazazi, P. Pearce and H. A. Stone, *Phys. Rev. Fluids*, 2024, **9**, L032301.

45 J. Happel and H. Brenner, *Low Reynolds Number Hydrodynamics: With Special Applications to Particulate Media*, Springer Science & Business Media, 2012, vol. 1.